Journal of Alloys and Compounds 829 (2020) 154508

Contents lists available at ScienceDirect

Journal of Alloys and Compounds

journal homepage: http://www.elsevier.com/locate/jalcom

Turning the activity of Cr–Ce mixed oxide towards thermocatalytic NO oxidation and photocatalytic CO_2 reduction via the formation of yolk shell structure hollow microspheres

Yunxia Zhao [a, 1], Wei Cai [a, b, 1], Mindong Chen [a], Yunfei Bu [a, *]

[a] Jiangsu Collaborative Innovation Center of Atmospheric Environment and Equipment Technology (CICAEET), Jiangsu Key Laboratory of Atmospheric Environment Monitoring and Pollution Control, UNIST-NUIST Research Center of Environment and Energy, School of Environmental Science and Engineering, Nanjing University of Information Science & Technology, Nanjing, 210044, PR China
[b] Datang Nanjing Environmental Protection Technology Co., Ltd, Nanjing, 21111, PR China

ARTICLE INFO

Article history:
Received 13 August 2019
Received in revised form
25 November 2019
Accepted 24 February 2020
Available online 25 February 2020

Keywords:
Cr-Ce mixed oxides
Double-shelled hollow structure
Multifunctional catalysis
Low-temperature NO oxidation
CO_2 photocatalytic reduction

ABSTRACT

Cr–Ce mixed oxides microspheres will have considerable potential in thermocatalytic NO oxidation and photocatalytic CO_2 reduction reaction (CO_2RR) if their low porosity and expensive synthetic expenditure can be overcome. To avoid these obstacles, a facile and economical strategy was adopted to synthesize double-shelled hollow Cr–Ce mixed oxide microspheres. The highly active multipurpose catalyst achieved an ultrahigh thermocatalytic NO oxidation efficiency at low temperatures, and provided high yields of CH_4 and CH_3OH during the photocatalytic CO_2RR. For NO oxidation, the optimized catalyst provided over 40% NO removal at 150 °C, which was ascribed to the reduced aggregation of the active subunits and the increased active species availability. Further, the exposed surface could generate an increased content of Cr^{6+} and O_β, which played the key role in NO oxidation. For CO_2 photocatalytic reduction, the superior behavior originated from the reduced band gap and the effective separation of photoinduced charge carriers. This study opens up new possibilities of using Cr–Ce mixed oxides for application in catalysis.

1. Introduction

The structural and morphological control of nanomaterial catalysts with the goal of altering their physicochemical properties has become a popular approach in catalytic reactions [1]. In recent years, catalysts with a hollow structure have attracted significant attention. Lai et al. synthesized metal oxides (NiO, Co_3O_4, CuO, ZnO, $ZnFe_2O_4$) with a hollow structure using a carbonaceous microsphere as the template; the number and composition of shells could be adjusted by changing the heating conditions and concentration of the precursor solution [2]. The single, binary, ternary, quaternary and quinary component-containing composites were constructed by adopting a scalable spray pyrolysis strategy, and the results showed that the generation of an intermediate carbon-metal-oxide with a spherical shape was a crucial step [3]. Up-to-quadruple-shelled Co_3O_4 was synthesized by introducing ZIF-67 as the template, and the formation of a multi-shell structure was attributed to the topologic arrangement of metal atoms in metal-organic frameworks [4]. There are four major categories of synthesis methods for a multishelled hollow structure: hard-templating, soft-templating, self-templated, and template-free strategies. The preparation of catalysts with this special structure has great potential for various applications such as in photocatalysis, electrocatalysis, sensors, lithium-ion batteries, and drug delivery [5–9]. Among the metal oxide catalysts, CeO_2, a significant catalyst with an abundance of surface oxygen defects, has been thoroughly developed for heterogeneous catalytic reactions such as photocatalysis [10], de-NO_x [11], CO oxidation [12], and water-gas shift reactions [13]. The construction of CeO_2 with a hollow structure was recently reported [14–16], implying that a microreactor could be established by changing the morphology of the catalyst, thereby enhancing the catalytic performance. However, the methods employed for the formation of CeO_2 with a hollow structure are either prohibitively expensive or immensely complicated, hindering industrial applications. For instance, Sasidharan et al. synthesized CeO_2 with a hollow nanosphere morphology by using a very expensive

* Corresponding author.
E-mail address: jpu441@yahoo.com (Y. Bu).
[1] Dr. Yunxia Zhao and Dr. Wei Cai contributed this work equally.

https://doi.org/10.1016/j.jallcom.2020.154508
0925-8388/

additive, polymeric micelle poly(styrene-block-acrylic acid-block-ethylene oxide) [17]. In addition, Yoon et al. adopted polystyrene as a template to prepare CeO_2 hollow fibers, but the template required a complicated pretreatment regime [18]; furthermore, the lattice integrality of the bulk CeO_2 made it difficult for the shell to bypass the reactant during the catalytic reaction whereas a hollow structure would promote it. The creation of pores in the shell is another technique that has gradually emerged to enhance the permeability of the shell [19,20]; however, it is not possible to accurately regulate the permeability of the shell using current pore-forming methods.

The addition of a heteroatom into the CeO_2 lattice can promote its catalytic activity. For example, Zhang et al. explored the Cu-doped CeO_2 effect on the promotion of CO oxidation [21]. Y-doped CeO_2 nanorods displayed high activity for the degradation of model organic dyes under room temperature [22]. Xu et al. investigated the influence of doped $Ce_{1-x}M_xO$ catalysts (M = Sn, Al, Mn, Ni, and Zr) with a mesostructure on the oxidative dehydrogenation of ethylbenzene into styrene, and the results showed that 10 mol% Ni doping had the highest performance [23]; Notably, an obvious difference in the radius of a Ce atom and a heteroatom could change the CeO_2 lattice structure significantly; this difference was determined to be the main factor influencing the catalytic performance.

Based on the superiority of the hollow structure and the heteroatom doping of CeO_2 for the catalytic performance, numerous investigations on the synthesis of heteroatom-doped CeO_2 with a hollow structure have been recently conducted. For instance, with the uniform distribution of active species and abundant Mn^{4+} content, hollow MnO_x-CeO_2 nanotubes exhibited a high NO_x removal efficiency at low temperatures for the NH_3 selective catalytic reduction (SCR) reaction [15]. Hollow MnO_x-CeO_2 mixed oxides were also synthesized for NO oxidation at low temperatures [24], and a similar conclusion was obtained regarding the high dispersion of MnO_x on CeO_2 and a greater amount of high-valence Mn as a result of the hollow structure. Similar hollow microspheres of Ce-based catalysts were reported for CO oxidation at low temperature, and the enhanced catalytic performance was attributed to the formation of a hollow structure to promote the interaction between CeO_2 and heteroatom, thus generating more active oxygen on the surface [25–27]. However, for the de-NO_x reaction, the existence of SO_2 could inactivate the catalyst by forming stable sulfate on the surface. Previous study indicated that the introduction of Cr could suppress the generation of sulfate, thus enhancing the de-NO_x efficiency in the presence of SO_2 [28]. In addition, a CdS/CeO_2 core/shell composite showed enhanced photocatalytic CO_2 reduction activity due to the low recombination rate of photogenerated electron/hole pairs, which was caused by the formation of a type II heterojunction at the core/shell interface [29]. However, the synthesis of hollow-structured Ce-based catalysts for multiple catalytic reactions has not been reported, and little research has been performed on Cr–Ce catalysts with hollow structures.

In this work, Cr–Ce mixed oxides with hollow structures were synthesized via a simple one-pot method and were evaluated via multiple catalytic reactions including thermocatalytic NO oxidation reaction and CO_2RR. The amount of Cr doping into the CeO_2 lattice was controllable in this technique; thus, the degree of distortion of the lattice structure could be controlled artificially. The permeability of the shell was controlled by changing the amount of Cr doping, thereby promoting the NO oxidation ability at low temperatures. The oxidation efficiency was 42% at 150 °C and reached 50% at 170 °C. In addition, due to the controllable degree of distortion of the shell, the compositions of the products could also be controlled when the catalysts were applied for CO_2 photocatalysis. The product consisted only of CH_4 when the Cr doping was lower than 5% whereas the products were composed of both CH_4 and CH_3OH when the Cr doping was 7% or greater.

2. Experimental procedure

2.1. Catalyst preparation

Details on the preparation are presented in Note 1 in the supporting information. The synthesized samples were denoted as *x*CCE-U*y*1, where *x* and *y* represent the Cr doping amount and the mole ratio of urea, respectively. Catalysts without Cr doping or urea were also prepared for comparison and were labeled CE-U31 or 10CCE, respectively.

2.2. Characterization

Details on the characterization are shown in Note 2 in the supporting information.

2.3. Catalytic oxidation test of NO

A catalytic oxidation test of NO at atmospheric pressure was carried out in a fixed bed reactor. Its key part is a quartz tube with an inner diameter of 6.8 mm. Before each test, 300 mg catalyst (40–60 mesh) was loaded in it with quartz wool blocking both ends. A gas mixture of 400 ppm NO, 8 vol% O_2 and N_2 as the balance gas was passed through the catalyst bed at a gas hour space velocity (GHSV) of 35,400 h^{-1}. A 90-min reaction was isothermally tested every 50 °C from 150 °C to 400 °C. The gas products were analyzed by a flue gas analyzer (Ecom-JZKN, Germany) and NO conversion was determined according to the following equation:

$$\text{NO conversion to } NO_2 = (NO_{in} - NO_{out}) / NO_{in} * 100\%$$

2.4. Density functional theory (DFT) calculations

Using the software package DMol3 [30,31], the exchange and correlation energies were investigated based on spin-polarized DFT calculations treated within the generalized gradient approximation (GGA) using the Perdew-Burke-Ernzerhof (PBE) functional [32]. The Brillouin zone was sampled by the Monkhorst-Pack $4 \times 4 \times 1$ grid. A Fermi smearing of 0.1 eV was utilized. The convergence criteria used for the geometry optimizations were 10^{-5} eV and 0.002 eV $Å^{-1}$ for the total energy and forces acting on the ions, respectively.

2.5. Photocatalytic reduction test of CO_2

CO_2 photocatalytic reduction was conducted in a gas-closed circulation system by applying a 200 mL Teflon-lined stainless steel reactor (Anhui Kemi Machinery Technology Co., Ltd., China). First, 50 mg photocatalyst was uniformly dispersed into the black Teflon container with 15 mL deionized water, and the suspension was stirred during the reaction. The reactor was purified with high-purity CO_2 (99.99%) gas to the pressure of 0.6 MPa for the CO_2 photoreduction. Then, a 300 W Xe lamp (CEL-HXF300, Beijing CEAulight Co., Ltd., China) with a UV-light cut-off filter ($\lambda > 420$ nm) as the light source irradiated the sapphire at the top of the reactor. The temperature of the reactor was controlled at 60 °C via the circulating cooling water. After photoreaction for 6 h, the product in the reactor was injected into a gas chromatograph (GC-9860, Nanjing Hope Corp., China) slowly. The CH_4, CH_3OH, and other carbon-based gases were analyzed via a flame ionization detector (FID) equipped with a 5A molecular column and a TDX-01 packed column.

3. Results and discussion

Compared with the conventional syntheses of hollow-type CeO_2 structures, which require complicated, time-consuming, expensive templates [17], a one-pot technique for synthesizing CeO_2 hollow microspheres (adopting urea as a cheap template) is much more convenient. The synthesis process of Cr—Ce mixed oxides with a double-shelled hollow morphology is illustrated in Fig. 1A. The addition of urea has a surprising influence on the hollow structure [28]. The synthesized 10CCE-U31 hollow microspheres display a double-shelled structure in which four cores are located within the second shell. The effects of urea on the physical structure of the sample are shown in Fig. 1B, and C. Both 10CCE-U31 and 10CCE exhibit four main peaks corresponding to the CeO_2 cubic structure (JCPDS No. 34—0394) [33]. Two catalysts display similar patterns, indicating that the addition of urea did not influence the formation of crystal structures. Additionally, compared with pure CeO_2, the XRD peaks of both catalysts shift to higher angles. Because the radius of Cr^{3+} ($r_{Cr}^{3+} = 0.0615$ nm) is smaller than that of Ce^{4+} ($r_{Ce}^{4+} = 0.097$ nm), we conclude that the Cr was doped into the CeO_2 lattice. As listed in Table 1, 10CCE-U31 exhibits a higher BET surface area than 10CCE. In addition, the N_2 adsorption-desorption isotherms of both catalysts are different; 10CCE displays a type III isotherm with a type H3 hysteresis loop, whereas 10CCE-U31 displays a type IV isotherm with a type H4 hysteresis loop [34,35], as shown in Fig. S1. The SEM images reveal the differences in the BET surface areas of the two catalysts; the BET surface area of 10CCE is mainly generated by the aggregates of small nanospheres, whereas the BET surface area of 10CCE-U31 results from its hollow structure, thus the average pore size of 10CCE is higher than that of 10CCE-U31, as shown in Table 1. The above results indicate that the addition of urea mainly influenced the morphologies of Cr—Ce mixed oxides rather than the crystal structure.

The varying Cr content in CeO_2 was investigated to study its impacts on the structure of the mixed metal oxides. As shown in Fig. 2, with an increasing content of the Cr-containing precursor, obvious angle shifts appear for the 5CCE-U31, 7CCE-U31 and 10CCE-U31 samples in their XRD patterns. Moreover, there is no CrO_x peak among the catalyst peaks, which indicates that all Cr atoms were doped into the CeO_2 lattice. The N_2 adsorption-desorption isotherms of the catalysts with different Cr doping amounts are shown in Fig. S2A. The catalysts all exhibit type IV isotherms with type H4 hysteresis loops, indicating the existence of a narrow stenopaic pore structure [35]. The BET results are illustrated in Table 1, displaying that the surface area, pore volume and pore size increased as the Cr doping increased. These findings indicate that the addition of Cr atoms in conjunction with Ce atoms was beneficial for the generation of pores during the hydrothermal process, confirming the results of a previous study [36]. Additionally, the increase in Cr doping could enlarge the pore size. SEM images of the *x*CCE-U31 series catalysts are shown in Fig. 3A. The varying Cr doping did not obviously influence the morphologies of the catalysts. However, all catalysts display the obvious double-shelled shape in the TEM images (Fig. 3B). The number of particles attached to the outmost shell increased as the Cr doping increased, which is attributed to the expansile pore structure caused by Cr doping. Combined with the BET results, the generated pores on the shell could facilitate the transport of reactants and increase the number of the exposed active sites, thereby promoting the catalytic performance.

The surface element valence state over the catalysts with varying Cr doping was analyzed by XPS characterization, as shown in Fig. 4. The survey spectra confirm the survival of Ce, Cr, and O in the catalysts. In the 2p3/2 region of the Cr 2p spectra, all catalysts are fitted into Cr^{3+} and Cr^{6+} states, which are assigned to the Cr_2O_3 species and CrO_3 species, respectively. The peak with the highest binding energy is attributed to the Cr^{6+} species and the other peaks correspond to the Cr^{3+} species [37]. The 3d spectrum of Ce is fitted into eight peaks in several different regions (3d5/2: v series, 3d3/2: u series) via Gaussian fitting, in which the peaks labeled *v*, *v*'', *v*''' and *u*, *u*'', *u*''' are assigned to the Ce^{4+} state and the *v*' and *u*' peaks are attributed to the Ce^{3+} state [38]. Two main peaks can be separated after fitting for the O 1s spectra: one peak is denoted O_α, corresponding to the lattice oxygen (O^{2-}) at a lower binding energy, and the other is denoted O_β, corresponding to the chemisorbed oxygen, such as O_2^- or O^- at a higher binding energy [39]. From the Cr 2p spectrum, the peak intensities and ratios of Cr^{6+} to Cr^{3+} increase with an increase in the Cr doping. Because Cr possesses a higher electronegativity than Ce, a shift in the Cr^{3+} peak appears in 10CCE-U31 with the replacement of Ce by Cr. The Cr 2p and O 1s spectra show that 10CCE-U31 exhibits the highest Cr^{6+} and O_β content, as shown in Table 2. In the Ce-containing catalysis system, the variation trends in the Ce^{3+} and O_β contents have the same characteristics. In conclusion, based on the strong oxidizability of Cr^{6+} and O_β, the doping of Cr into CeO_2 clearly enhanced the oxidizing ability of the catalysts. The influence of the Cr doping into CeO_2 on the electronic structure was further studied by DFT theoretical calculations, as shown in Fig. S3. The replacements of the Ce atom in the lattice cell by one Cr atom and two Cr atoms were calculated, which represented 5% and 10% Cr doping in moles, respectively. The results show that the electron transport capacity was enhanced after doping with one Cr atom. The same phenomenon was further confirmed after doping with two Cr atoms. The calculation results were similar in the XPS analysis.

The influence of different urea dosages on the physicochemical structure of the catalysts was also investigated, as shown in Fig. S2B and Fig. S4. The catalysts with different urea dosages display similar XRD patterns; they all shift to higher angles than that of pure CeO_2. Additionally, an obvious impurity phase appears over the catalysts with a greater addition of urea. These series catalysts also exhibit a similar N_2 adsorption-desorption isotherm type, and 10CCE-U31 possesses the highest surface area and pore volume. The SEM images confirm the XRD results, displaying a similar morphology with a double-shelled hollow structure under different urea dosages. The surface element valence states over three typical catalysts 10CCE-U*y*1 ($y = 1, 3, 5$) were characterized via XPS, as shown in Fig. S5. The peak fitting processes of Cr 2p, Ce 3d and O 1s over the catalysts with different urea dosages are the same as those in the above XPS analysis. However, the fitting results, such as the Cr^{6+} and O_β ratios, are different. The optimal urea dosage for the preparation of the double-shelled hollow Cr—Ce mixed oxides is based on the Cr^{6+} and O_β content. The specific Ce^{3+}, Cr^{6+} and O_β content on the surface of the catalysts are listed in Table 2. The results show that 10CCE-U31 exhibits the highest Ce^{3+}, Cr^{6+} and O_β content among the three catalysts; thus, it possesses a relatively high oxidizing ability.

SEM images of 10CCE-U31 at different resolutions are shown in Fig. S6. Double-shelled hollow microspheres are clearly observed. The particle sizes are concentrated over 1.5 μm, and the average particle size is 2.25 μm.

A typical TEM image of 10CCE-U31 is displayed in Fig. 5A, which clearly confirms its double-shelled hollow structure. As exhibited in the HRTEM image (Fig. 5B), 10CCE-U31 nanocrystal subunits in the shell with an interplanar spacing of 0.321 nm matches the (1 1 1) crystallographic plane of cubic CeO_2. The selected area electron diffraction (SAED) image (Fig. 5C) of 10CCE-U31 displays four main continuous rings corresponding to the (1 1 1), (2 0 0), (2 2 0) and (3 1 1) planes of CeO_2 in accordance with the XRD analysis. The uniform distribution of each element in every shell and the cores of the Cr—Ce mixed oxide hollow microspheres investigated by energy-

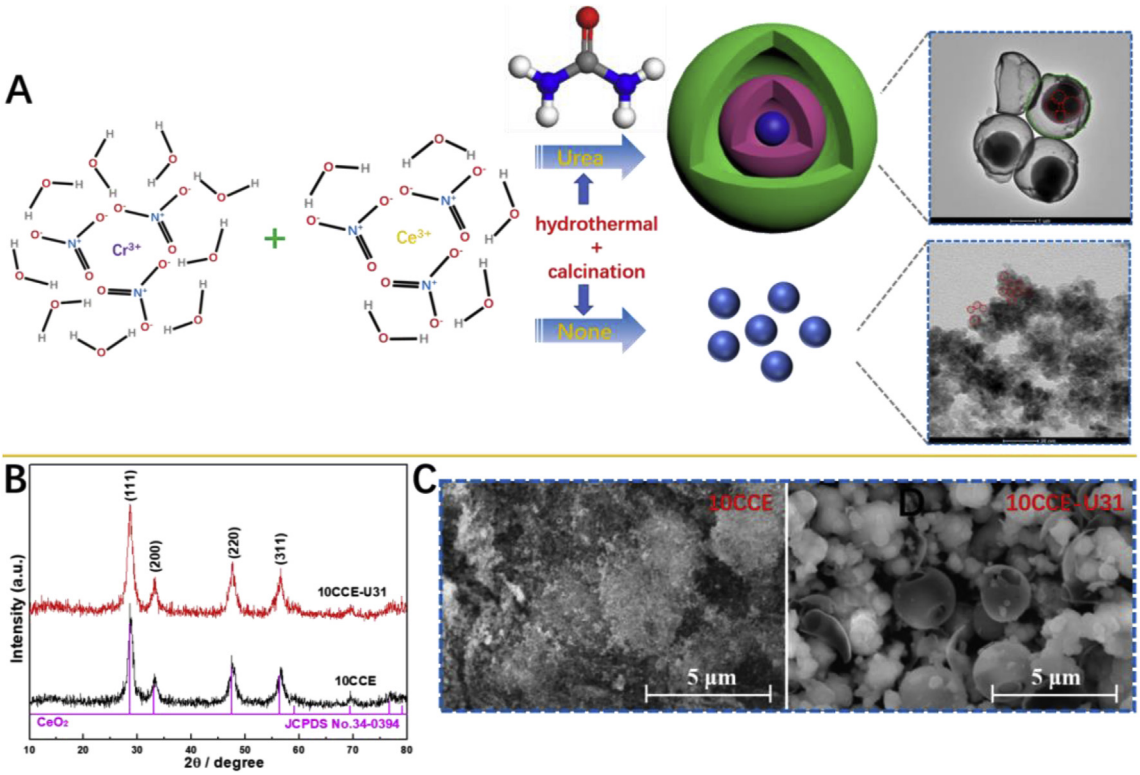

Fig. 1. Schematic formation process (A), XRD patterns (B) and SEM images (C) of Cr–Ce mixed oxides with and without the addition of urea.

Table 1
The BET surface area and pore structure of the *x*CCE-Uy1 series catalysts.

Sample	BET surface area (m^2/g)	Pore volume (mm^3/g)	Pore size (nm)
10CCE	111.8	541.8	10.9
3CCE-U31	56.4	72.9	3.32
5CCE-U31	63.1	84.2	4.62
7CCE-U31	103.5	127.1	4.79
10CCE-U31	160.9	186.2	5.34
10CCE-U11	114.4	94.8	4.91
10CCE-U21	124.2	149.1	4.95
10CCE-U41	134.9	182.7	5.42
10CCE-U51	119.5	147.8	5.17

dispersive X-ray spectroscopy (EDX) element mapping is shown in Fig. 5D.

The formation mechanism of the double-shelled hollow structure was discussed and confirmed by characterizations. SEM and TEM images of the uncalcinated 10CCE-U31 sample are shown in Fig. S7, and the results show that, before calcination, a single-shelled hollow sample was formed during the hydrothermal process. The XRD pattern and EDX element mapping of the uncalcinated sample were determined, as shown in Fig. S8. The XRD results show that the uncalcinated sample is similar to the calcined catalyst, and the EDX mapping results show that the Cr, Ce and O

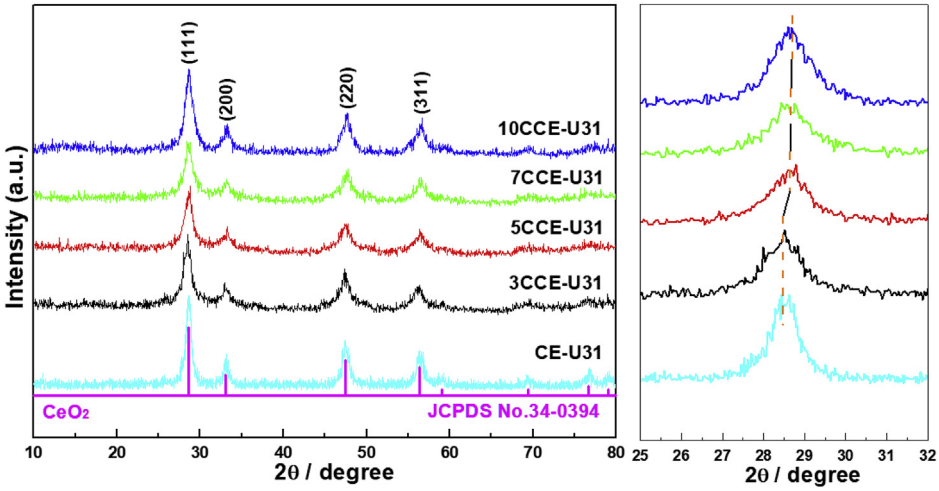

Fig. 2. XRD patterns of the *x*CCE-U31 (x = 0, 1, 3, 5, 7, 10) series catalysts.

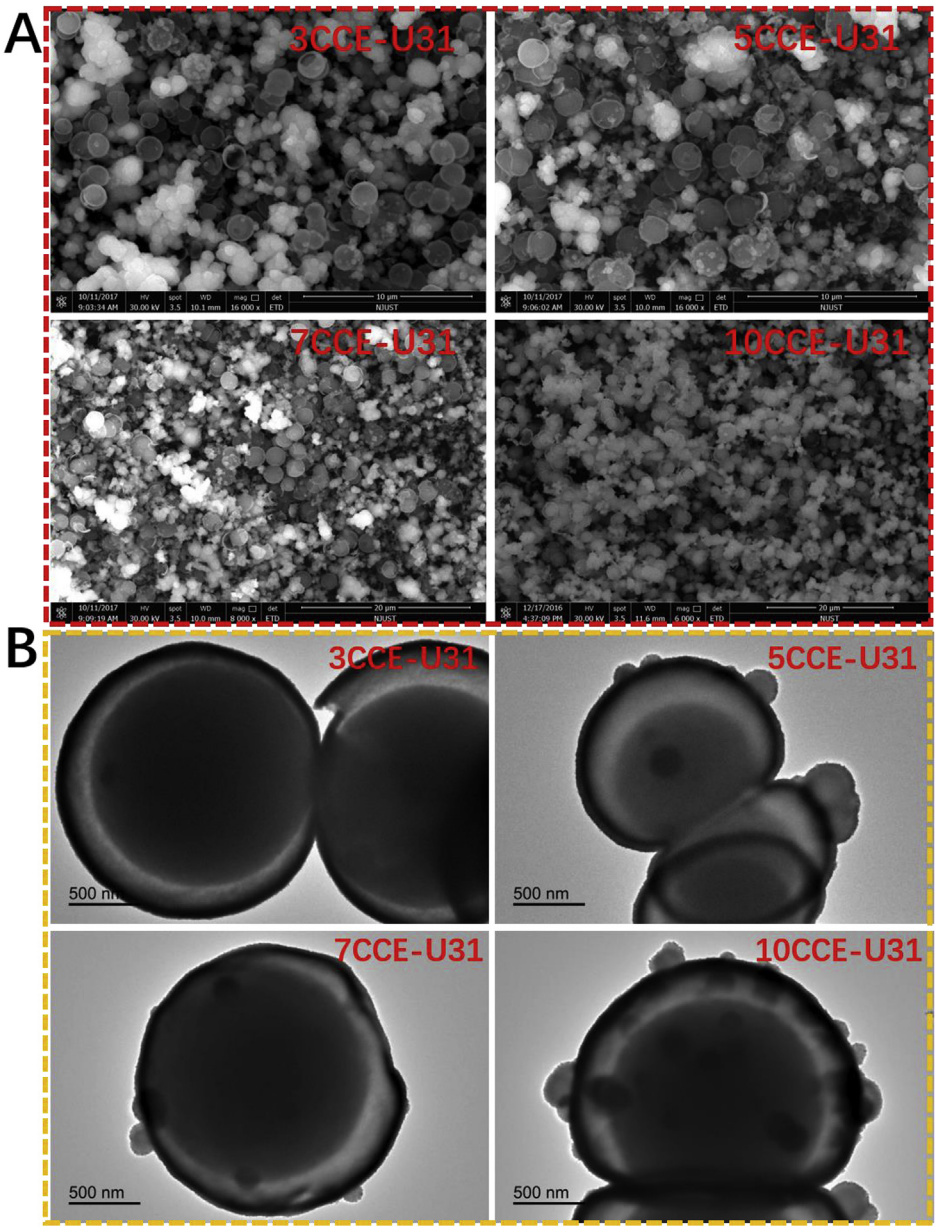

Fig. 3. (A) SEM images and (B) TEM images of the *x*CCE-U31 (x = 3, 5, 7, 10) series catalysts.

elements are well dispersed in the hollow microsphere. These results indicate that the structure of CeO_2 was formed during the hydrothermal process, and Cr was doped into CeO_2 lattice uniformly. Combined with the TEM images of the calcined sample, it could be concluded that a primary core-shell structure was generated after hydrothermal treatment, and the calcination process was the key step in forming the double-shelled hollow structure.

As shown in Fig. 6A, H_2 -TPR was used to characterize the active sites on the surfaces of the catalysts. Several reduction peaks are found over all catalysts at the range of 100–600 °C. The reduction of surface ceria oxide appears in the low-temperature region (I, 260–400 °C) and the reduction of Cr^{6+} (Cr^{6+} to Cr^{3+}) appears in the high-temperature region (II, 410–570 °C) [40,41]. The catalysts with high Cr doping display high reduction peaks in areas I and II, and 10CCE-U31 exhibits the highest reduction. The results indicate that an increase in the Cr doping could benefit the interactions between Cr and Ce species, thereby generating additional active sites. The appropriate addition of urea could further enhance these interactions. The TPR results are consistent with the XPS analysis. For the gas-phase reaction, the reactant adsorption capacity of the catalysts plays an important role. The NO and O_2 adsorption properties of all catalysts were tested by TPD experiments, as shown in Fig. 6B and C. From the NO-TPD profiles, two desorption peak regions are derived: the peak in the low-temperature area (α peak) is attributed to the monodentate nitrate and bridged nitrate, and others at high temperature (β peak) can be assigned to the bridged nitrate and bidentate nitrate [42]. The catalysts with higher Cr doping display low α peak temperatures, indicating that these catalysts possess high NO adsorption capacities at low temperatures. Among the catalysts, 10CCE-U31 exhibits the highest α peak area, which might be due to its high Cr^{6+} content. In the O_2-TPD results, three oxygen species are obtained in three separate temperature regions. The peak lower than 400 °C (δ peak) is caused by a

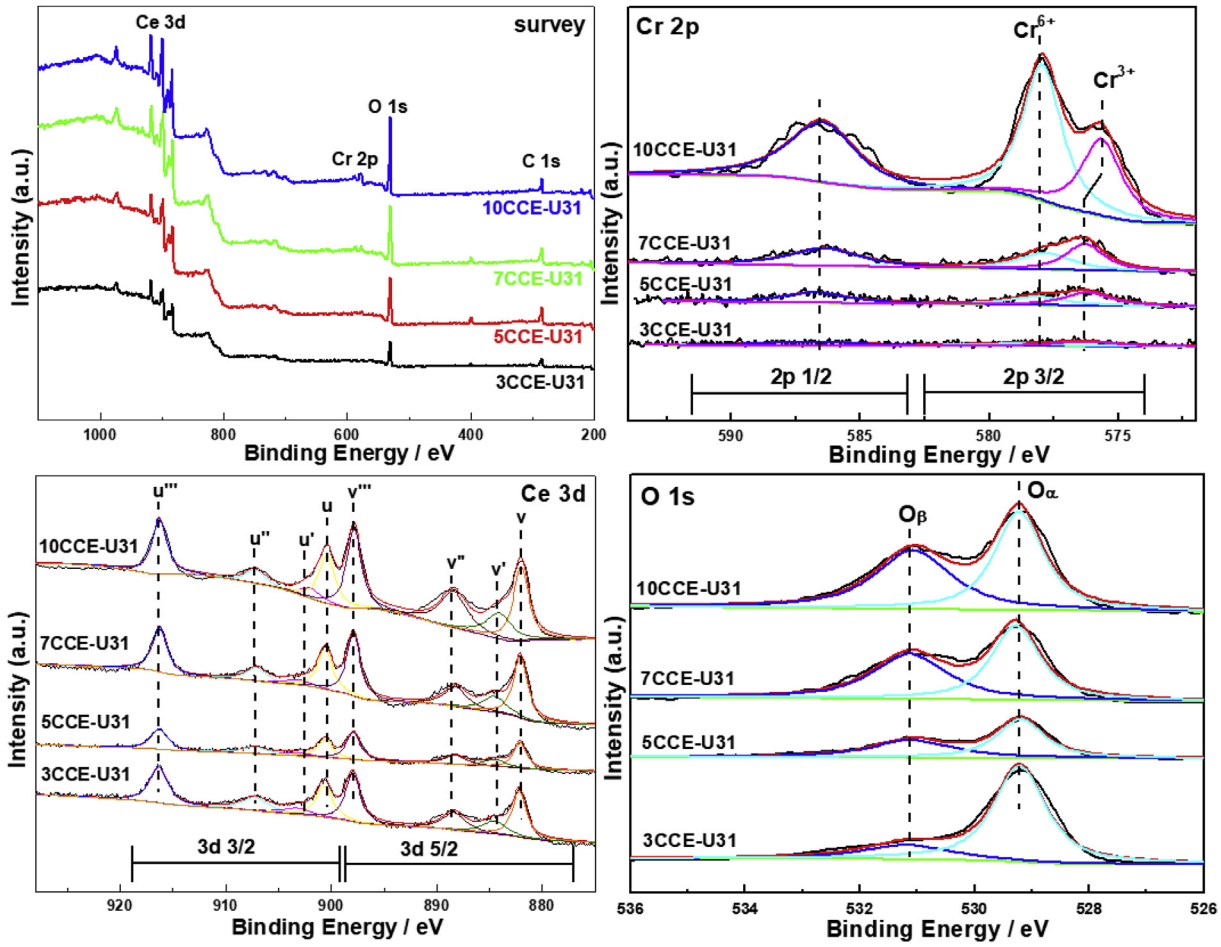

Fig. 4. XPS (survey, Cr 2p, Ce 3d, O 1s) of the *x*CCE-U31 (x = 3, 5, 7, 10) series catalysts.

Table 2
XPS elementary cation surface concentrations of the *x*CCE-U*y*1 series catalysts.

Sample	Cation ratios		
	$Cr^{6+}/Cr_{(total)}$	$Ce^{3+}/Ce_{(total)}$	$O_\beta/(O_\alpha+O_\beta)$
10CCE	55.19%	9.43%	64.90%
3CCE-U31	53.11%	12.04%	32.08%
5CCE-U31	53.46%	12.48%	48.17%
7CCE-U31	57.14%	13.72%	54.24%
10CCE-U31	63.01%	15.37%	58.31%
10CCE-U11	51.45%	10.21%	30.04%
10CCE-U51	52.09%	10.82%	30.14%

kind of physically and weakly chemically adsorbed oxygen, and the peak higher than 550 °C (γ peak) is attributed to the oxygen in the lattice. The peak between the δ peak and ε peak is derived from the oxygen defects (ε peak), generally existing in the form of chemisorbed oxygen such as O^- and O_2^- [43]. The results show that 10CCE-U31 possesses the highest δ peak and ε peak areas, indicating the abundance of chemisorbed oxygen on the surface in accordance with the XPS results. NO oxidation was carried out over all catalysts in the temperature range of 150–400 °C to test the oxidizability, as shown in Fig. 6D. The catalytic activity over all catalysts first increases and then decreases with increasing temperature. The decrease in the oxidation activity at higher temperature is attributed to the limitation of thermodynamic equilibrium [44]. Moreover, the oxidation efficiency increases with increased Cr doping, especially in the low-temperature region (150–200 °C). Based on the oxidation performance, there is an optimum addition of urea that is three times the total metallic element content in the mole ratio. The NO oxidation results match the abovementioned XPS, TPR and TPD results. Among the catalysts, 10CCE-U31 exhibits the highest NO oxidation performance in the tested temperature region, and its highest oxidation activity is 83.3% at 300 °C. Notably, 10CCE-U31 also displays excellent low-temperature activity. The efficiency reaches 42.8% at 150 °C and 59.9% at 200 °C, and the temperature point for an NO oxidation efficiency of 50% is 170 °C; thus, 10CCE-U31 can satisfy the changes in the oxidation process after the desulfurization system to a certain degree. Moreover, the oxidation activities over most samples are in accordance with the thermodynamic equilibrium, excluding 10CCE-U21, 10CCE-U31, 10CCE-U41 and 10CCE-U51 at high temperature over 300 °C, which all have 10% Cr doping. This phenomenon is attributed to the high oxidation efficiency caused by Cr active species, which was confirmed in our previous work [45]. In addition, the stability of the optimized catalyst 10CCE-U31 was tested. As shown in Fig. S9, 10CCE-U31 displays stable NO oxidation efficiency under 300 °C. Moreover, three "cooling and heating" cycling tests also confirmed the excellent stability of 10CCE-U31.

To investigate the NO oxidation at lower temperatures, 10CCE-U31 was exposed to a gas mixture of 1000 ppm NO and 8 vol% O_2, and the temperature was increased to 250 °C at an interval of 50 °C in the *in situ* diffuse reflectance infrared Fourier transform spectroscopy (DRIFTS) technique system. The spectrum was collected at

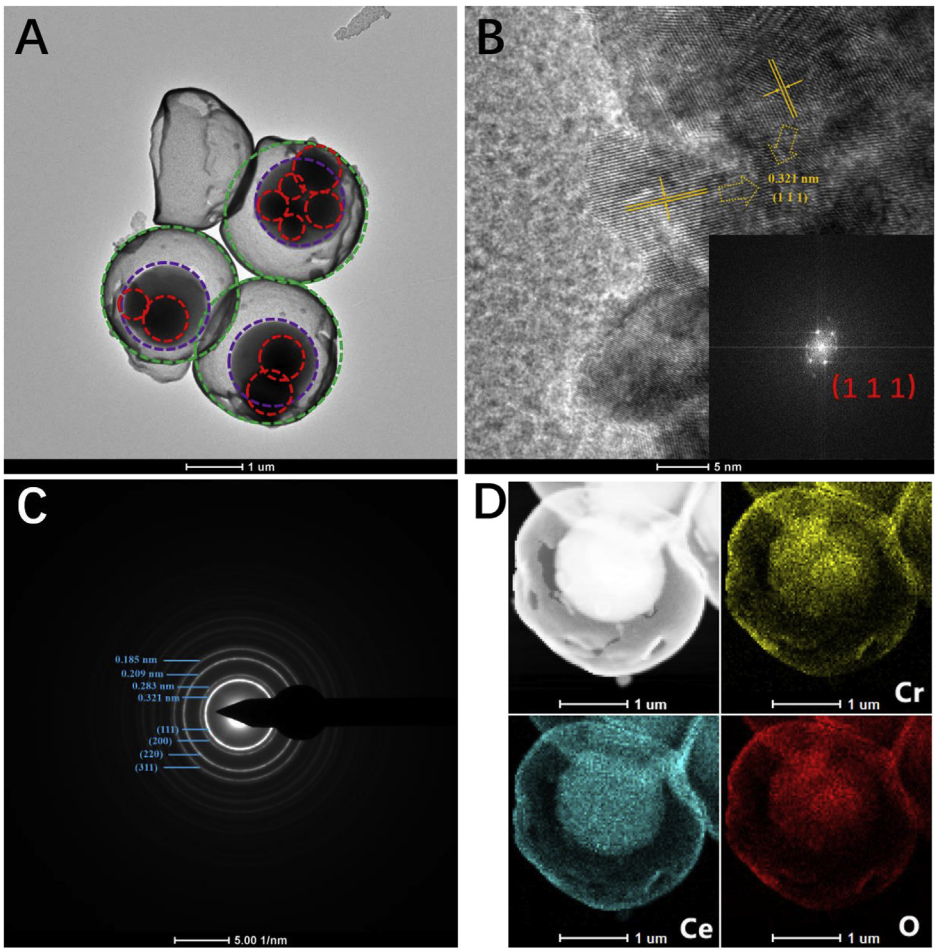

Fig. 5. TEM image (A), HRTEM image (B) (small figure is a fast Fourier transform image of a 10CCE-U31 particle), SAED image (C) and EDX element mapping (D) of the 10CCE-U31 catalyst.

5 min and 30 min for each temperature, as shown in Fig. S10. Four typical bands were detected. First, the band at 1258 cm^{-1} can be attributed as bridged nitrate [46], and the band at 1043 cm^{-1} is assigned to monodentate nitrate [47]. The band at 1353 cm^{-1} is attributed to the adsorbed NO_3^-, which can be formed by the interaction between chemisorbed NO and O_2^- [48]. The band at 1400 cm^{-1} is assigned to the intermediate NO^+ [49]. The intensity of the bridged nitrate decreases with increasing temperature, and the intensities of the other three bands begin to increase at the same time. Among these bands, an intensity increase of the monodentate nitrate and adsorbed NO_3^- appears when the temperature increases to 200 °C, and an intensity increase of intermediate NO^+ appears at 250 °C. These results confirm that the 10CCE-U31 catalyst possesses catalytic oxidation ability at low temperatures. We propose a NO oxidation mechanism over 10CCE-U31 based on the above analysis, as shown in Scheme 1. The adsorbed NO_3^- can react with the intermediate NO^+ to generate two NO_2 molecules.

The surface electronic states and the band gap were obtained via UV–vis DRS measurements, as shown in Fig. 7A. Two typical absorption bands centered at 270 nm and 360 nm can be found in all the catalysts. These two bands are caused by $Ce^{4+} \leftarrow O^{2-}$ charge transfer (270 nm) and interband (360 nm) transitions [50,51]. No clear absorption band corresponding to the $Ce^{3+} \leftarrow O^{2-}$ charge transfer transition is observed, which generally appeared at 255 nm [52]. In addition, the bands attributed to Cr^{3+} and Cr_2O_3 are usually centered at ~460 nm and ~590 nm, respectively [53], but they were not found over all catalysts. These results confirm that there are few CrO_x species on the surface and that Cr is doped into the CeO_2 lattice. Based on the adsorption band edge, the band gap (*Eg*) of each catalyst was calculated, as shown in the inset in Fig. 7A. The band gap decreases with increasing Cr doping and the 10CCE-Uy1 series catalysts display similar *Eg* values, indicating that the different quantities of added urea exhibit little influence on the band gaps. The band gaps of the catalysts are listed in Table S1. As shown in Fig. 7B, we used Mott-Schottky measurements to clarify the band structures of the catalysts. For n-type semiconductors, reversed sigmoidal plots are realized with an overall shape consistent with that type. The flat band potentials (V_{fb}) can be determined from the *x* intercept of the linear region, where the units are V *vs.* Ag/AgCl. Based on equation *E* (RHE, reversible hydrogen electrode) = *E*(Ag/AgCl) + 0.059 × pH + 0.195 V [54], V_{fb} was converted into the RHE potential. The pH of the electrolyte was measured as 6.8 at room temperature. In general, V_{fb} is close to the bottom of the conduction band (E_{CB}) of n-type semiconductors, which is just 0–0.2 V *vs.* RHE more negative than V_{fb} [54]. The band structures of the catalysts are summarized in Table S1. The E_{CB} values decrease with increasing Cr doping; furthermore, among the 10CCE-Uy1 series catalysts, 10CCE-U31 exhibits the lowest E_{CB} value. Commonly, a negative E_{CB} value is attributed to a stronger reducing capacity for the catalysis. Moreover, the catalysts possess the reduction potential to convert CO_2 into CH_4 or CH_3OH, according to Eqns. (1) and (2).

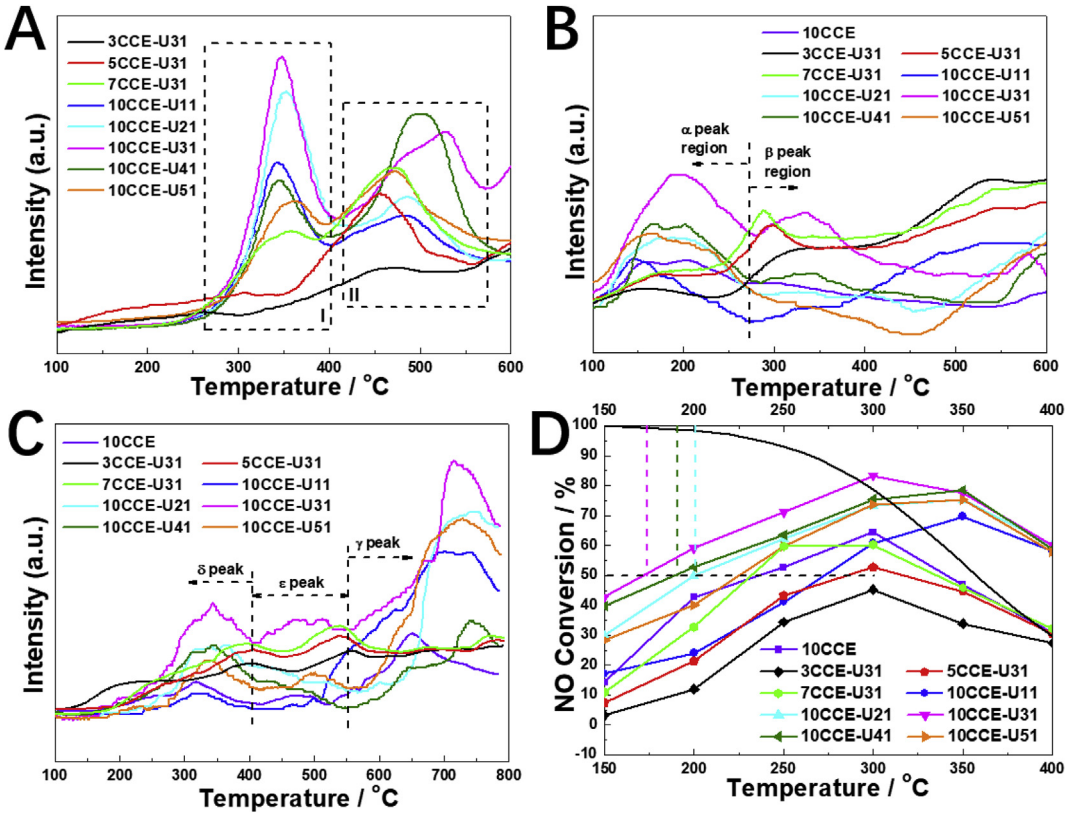

Fig. 6. H_2-TPR (A), NO-TPD (B), O_2-TPD (C) profiles of the *x*CCE-U*y*1 series catalysts. (D) NO catalytic oxidation performance of the *x*CCE-U*y*1 series catalysts.

$$CO_2 + 8H^+ + 8e^- \rightarrow CH_4 + 2H_2O \; E^0(V) = -0.24 \text{ eV} \quad (1)$$

$$CO_2 + 6H^+ + 6e^- \rightarrow CH_3OH + H_2O \; E^0(V) = -0.38 \text{ eV} \quad (2)$$

$$CO_2 + 2H^+ + 2e^- \rightarrow CO + H_2O \; E^0(V) = -0.53 \text{ eV} \quad (3)$$

An increased photocurrent density under visible light and a smaller diameter semicircular Nyquist curve observed in the electrochemical impedance spectroscopy (EIS) measurements can be associated with the separation of holes and photoinduced electrons [55], e.g., a low charge transfer resistance, and high separation of photogenerated electron-hole pairs [56]. As shown in Fig. 7C, the trend in the decrease in the radius is not linearly related to an increase in the Cr doping amount. This indicates the separation of photoinduced electrons and holes is also affected by the amount of urea added. A similar phenomenon was obtained in the photocurrent test in Fig. 7D; 10CCE-U31 shows the largest stable photocurrent density during on-off cycles of intermittent visible light irradiation compared with other catalysts. The photocatalytic performance of 10CCE-U31 was first investigated by the photodegradation of RhB, as shown in Fig. 8A. The fresh RhB solution without catalysts displays a main absorption peak at 554 nm, and the degradation efficiency over 10CCE-U31 increases as time progresses. A photo of the degradation results is shown in the inset in Fig. 8A. The photodegradation performance as a function of time over the catalysts is shown in Fig. 8B. The sequence of the degradation efficiency is in accordance with the EIS and photocurrent test results, and it is similar to the sequence of the BET surface area. This indicates that the separation efficiency of the photogenerated electron-hole pairs plays a key role in the photodegradation of RhB, although the BET surface area also plays an important role. The photocatalytic performance over the catalysts was also tested by the photoreduction of CO_2 with H_2O, as shown in Fig. 8C. CH_4 was generated over all catalysts, but CH_3OH formed only over the 10CCE-U*y*1 series catalysts. Combined with the results of Eqns. (1) and (2), whether CH_4 or CH_3OH could be generated over the catalysts was theoretically confirmed. Because the kinetic diameter of CH_3OH is greater than that of CH_4, the interaction between CO_2 and H_2O occurred inside the microsphere with a hollow structure and the generated CH_3OH was blocked by the shell. Doping with Cr could expand the CeO_2 lattice parameter; however, the catalysts with low Cr doping could not sufficiently expand the lattice to allow for CH_3OH to pass through. Hence, high Cr doping was necessary for the generation of CH_3OH. The trend of the generated CH_4 over the 10CCE-U*y*1 series catalysts was in accordance with that of the generated CH_3OH, confirming the above deduction. A graphic illustration is shown in Scheme 2. In addition, the sequence of the photoreduction activity is also in accordance with the EIS and photocurrent test results, confirming the key role of the separation efficiency of photogenerated electron-hole pairs during the photocatalytic test. The CH_4 and CH_3OH photocatalytic selectivity over the 10CCE-U*y*1 series catalysts is shown in Fig. 8D. 10CCE-U31 and 10CCE-U41 both exhibit a relatively high CH_3OH selectivity, indicating that the appropriate amount of added urea benefits the formation of CH_3OH. In addition, the undiscovered generation of CO occurred because the E_{CB} of most samples was more positive than the reduction potential of CO_2 to CO, based on Eqn. (3). Table S1 shows that 10CCE-U31 and 10CCE-U21 possessed the potential to reduce CO_2 to CO, but their conduction bands were both very close to the reduction potential; thus, they could not reduce CO_2 to CO, which may be caused by overpotential. The possible product of H_2 could not be detected because H_2 was applied as the carrier gas for FID detection.

Samples without the addition of urea were also prepared and

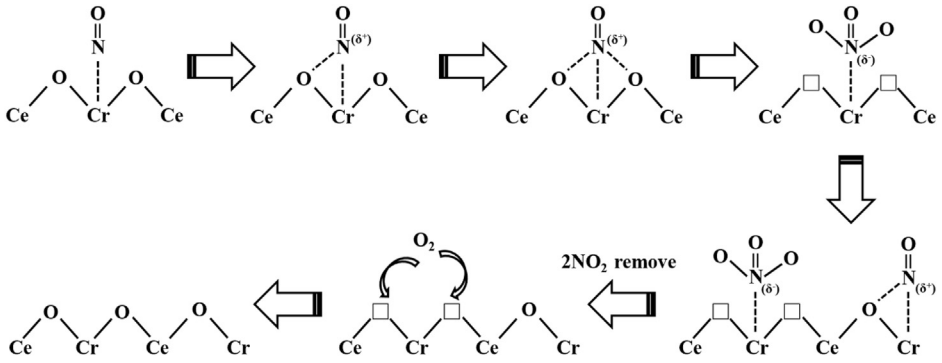

Scheme 1. Main pathway of NO oxidation over the 10CCE-U31 catalyst.

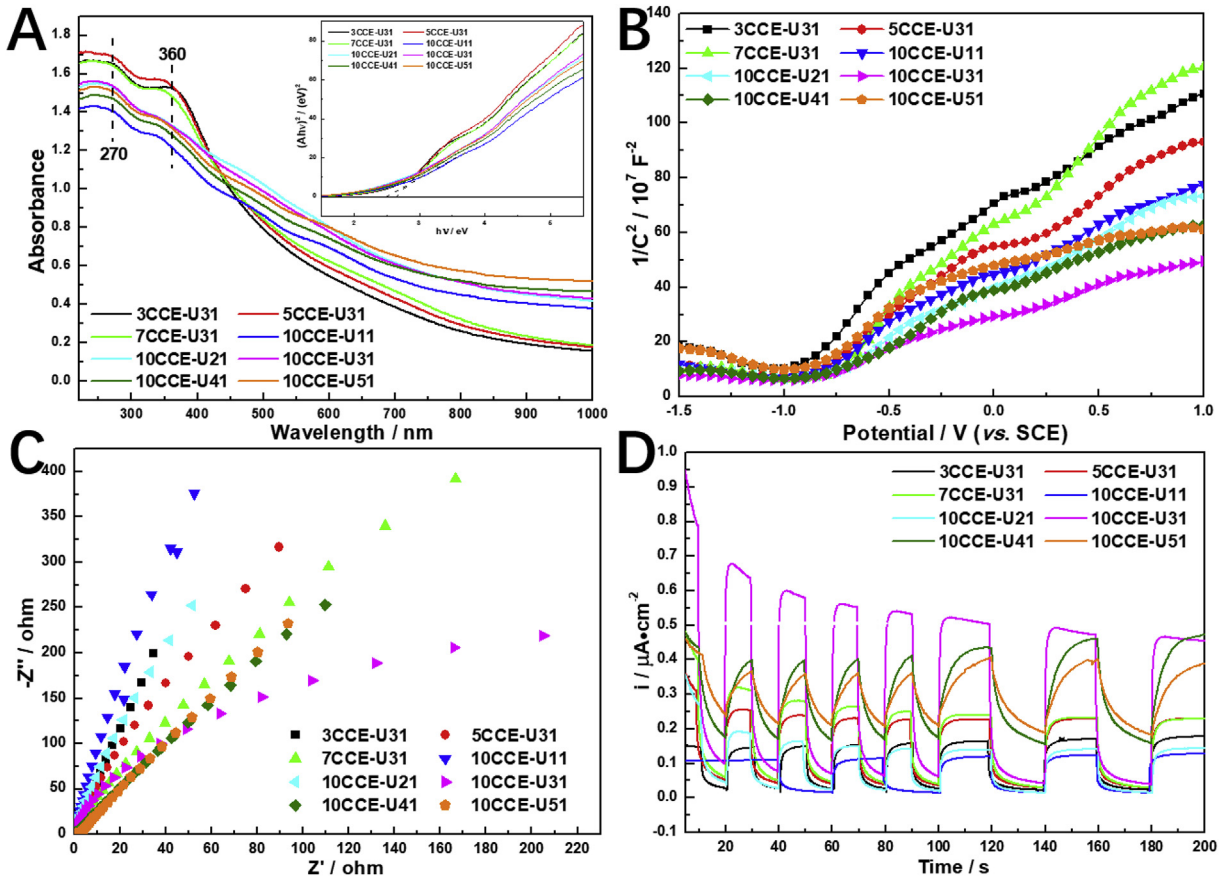

Fig. 7. UV−vis absorption spectra (A) (inset shows the band gap), Mott-Schottky plots (B), EIS Nyquist plots (C), and photocurrent potential curves (D) of the *x*CCE-U*y*1 series catalysts.

evaluated with CO_2RR for comparison and are displayed in Fig. S11. Three samples were named 3CCE, 5CCE and 10CCE, corresponding to the 3%, 5% and 10% Cr in mass ratio to CeO_2, respectively. The results showed that the CH_4 and CH_3OH yield amounts gradually increased with increasing Cr doping, exhibiting the same tendency as the urea-containing samples. This phenomenon confirmed that Cr doping could promote the generation of CH_4 and CH_3OH. However, compared with the urea-containing samples, CH_3OH was formed over the 5CCE sample, whereas no CH_3OH was found over 5CCE-U31. This occurred because the hollow structure was not formed in 5CCE and the generated CH_3OH could not be blocked as in the hollow-structured 5CCE-U31 sample; thus, CH_3OH could be still generated on the surface. Moreover, the appropriate addition of urea enhanced the generation of CH_4 and CH_3OH, attributed to the formation of a hollow structure with high Cr doping.

4. Conclusion

In summary, Cr−Ce mixed oxides with a double-shelled hollow structure were successfully synthesized via a simple one-pot method, for which use of cheap urea was adopted. The synthesized catalysts exhibited a remarkable performance in multifunction catalytic reactions, including thermocatalytic NO oxidation and photocatalytic CO_2 reduction, and the influence of different amounts of added Cr and urea on the catalytic performance was investigated. The XRD and DFT results showed that Cr atoms were

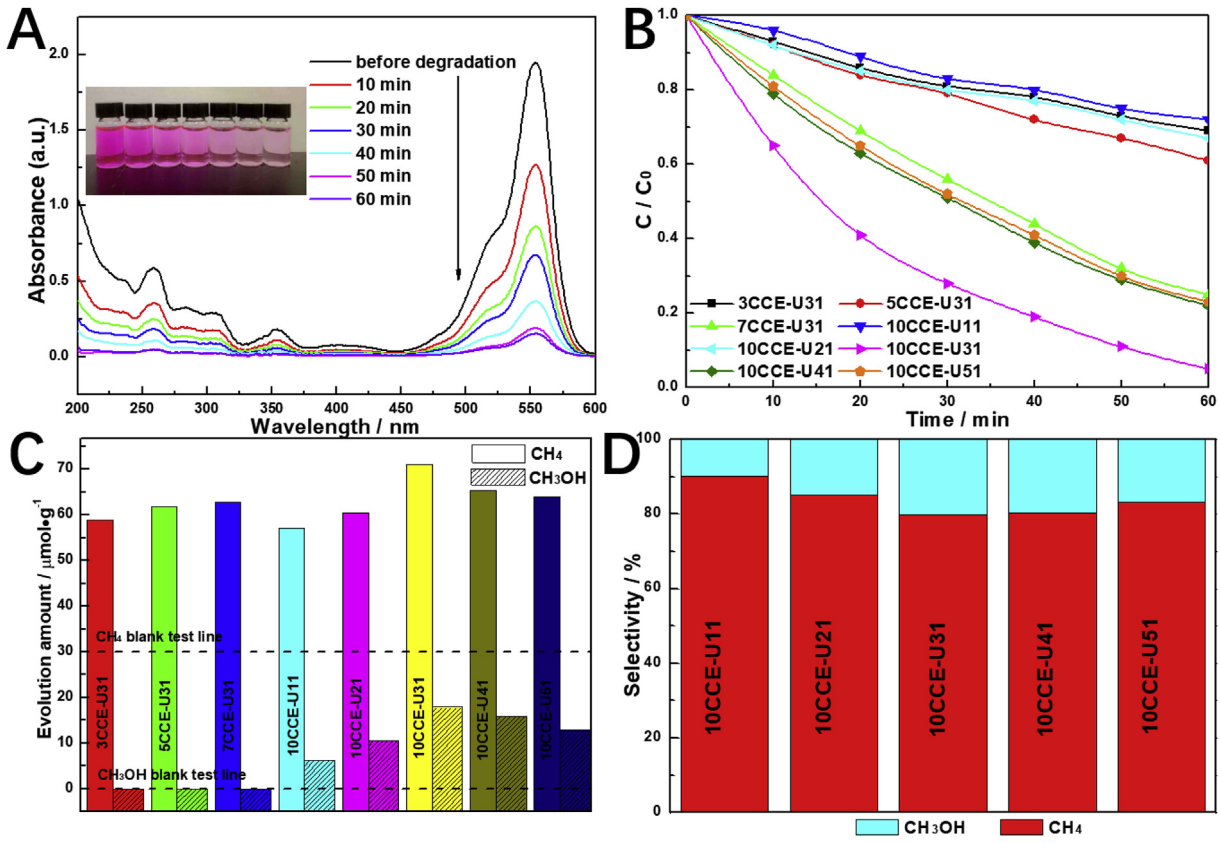

Fig. 8. (A) The absorbance of RhB over the 10CCE-U31 catalysts under visible light over time. (B) The relative concentration of RhB as a function of the illumination time for the *x*CCE-U*y*1 series catalysts under visible light. (C) Photocatalytic CH_4 and CH_3OH evolution performance and (D) the selectivity over the *x*CCE-U*y*1 series catalysts under visible light irradiation for 6 h.

doped into the CeO_2 lattice via substitution of Ce, and Cr species were well dispersed over the catalysts. The XPS and TPD results indicated that the obtained doped structures present in the hollow microspheres could generate additional lattice defects, increasing the Cr^{6+}, Ce^{3+} and O_β content on the surface, thereby enhancing the adsorption of NO and O_2 and improving the NO oxidation efficiency at low temperatures. Moreover, due to the hollow structure, photoinduced electrons and holes could be effectively separated, enhancing the photocatalytic CO_2RR, which resulted in high yields of CH_4 and CH_3OH during the reduction. Interestingly, due to the adjustable pore size on the shell caused by manual control of the Cr doping amount, the CH_4 and CH_3OH products could be automatically separated by the sample shell. This study opens new possibilities for using Cr—Ce mixed oxides in photocatalytic applications.

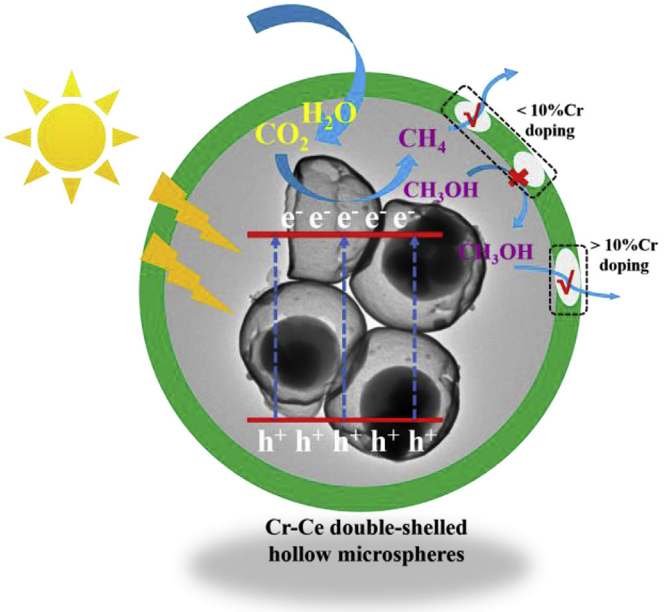

Scheme 2. Graphic illustration of the photocatalytic CO_2RR over Cr—Ce double-shelled hollow microspheres.

Author contribution statement

Yunxia Zhao: Investigation, Data Curation, Validation, Writing-Original draft, Writing- Reviewing and Editing. Wei Cai: Investigation, Formal analysis, Data Curation, Writing- Original draft, Writing- Reviewing and Editing. Mindong Chen: Supervision. Yunfei Bu: Conceptualization, Methodology.

Declaration of competing interest

The authors declare that they have no known competing financial interests or personal relationships that could have appeared to influence the work reported in this paper.

Acknowledgments

Dr. Yunxia Zhao and Dr. Wei Cai contributed to this work equally. This work was financially supported by the National Natural Science Foundation of China (51808296 and 51802160), the Natural

Science Foundation of Jiangsu Province of China (BK20170938 and BK20150892), the 63rd Chinese Postdoctoral Science Foundation (2018M630487), and the Startup Foundation for Introducing Talent of NUIST (2243141601034 and S8113082001). Wei Cai would like to acknowledge support and helpful discussion from the WECHAT group "Energetic and Progressive Mightyboy".

Appendix A. Supplementary data

Supplementary data to this article can be found online at https://doi.org/10.1016/j.jallcom.2020.154508.

References

[1] Z.W. Chen, W. Gao, W.T. Zheng, Q. Jiang, Steric hindrance in sulfur vacancy of monolayer MoS_2 boosts electrochemical reduction of carbon monoxide to methane, ChemsusChem 11 (2018) 1455–1459.
[2] X. Lai, J. Li, B.A. Korgel, Z. Dong, Z. Li, F. Su, J. Du, D. Wang, General synthesis and gas-sensing properties of multiple-shell metal oxide hollow microspheres, Angew. Chem. Int. Ed. 50 (2011) 2738–2741.
[3] Y.J. Hong, M.Y. Son, B.K. Park, Y.C. Kang, One-pot synthesis of yolk-shell materials with single, binary, ternary, quaternary, and quinary systems, Small 9 (2013) 2224–2227.
[4] L. Wang, J. Wan, Y. Zhao, N. Yang, D. Wang, Hollow multi-shelled structures of Co_3O_4 dodecahedron with unique crystal orientation for enhanced photocatalytic CO_2 reduction, J. Am. Chem. Soc. 141 (2019) 2238–2241.
[5] X. Lai, J.E. Halpert, D. Wang, Recent advances in micro-/nano-structured hollow spheres for energy applications: from simple to complex systems, Energy Environ. Sci. 5 (2012) 5604–5618.
[6] J. Qi, X. Lai, J. Wang, H. Tang, H. Ren, Y. Yang, Q. Jin, L. Zhang, R. Yu, G. Ma, Z. Su, H. Zhao, D. Wang, Multi-shelled hollow micro-/nanostructures, Chem. Soc. Rev. 44 (2015) 6749–6773.
[7] X. Wang, J. Feng, Y. Bai, Q. Zhang, Y. Yin, Synthesis, properties, and applications of hollow micro-/nanostructures, Chem. Rev. 116 (2016) 10983–11060.
[8] L. Yu, X.Y. Yu, X.W. Lou, The design and synthesis of hollow micro-/nanostructures: present and future trends, Adv. Mater. 30 (2018) 1800939–1800965.
[9] P. Zhang, X.W. Lou, Design of heterostructured hollow photocatalysts for solar-to-chemical energy conversion, Adv. Mater. 31 (2019) 1900281–1900298.
[10] W. Cai, Y. Shi, Y. Zhao, M. Chen, Q. Zhong, Y. Bu, The solvent-driven formation of multi-morphological Ag-CeO_2 plasmonic photocatalysts with enhanced visible-light photocatalytic reduction of CO_2, RSC Adv. 8 (2018) 40731–40739.
[11] W. Cai, Q. Zhong, D. Wang, Y. Zhao, M. Chen, Y. Bu, A rational design for enhanced catalytic activity and durability: strongly coupled N-doped CrO_x/$Ce_{0.2}Zr_{0.8}O_2$ nanoparticle composites, ACS Appl. Nano Mater. 1 (2018) 1150–1163.
[12] M. Lykaki, E. Pachatouridou, S.A.C. Carabineiro, E. Iliopoulou, C. Andriopoulou, N. Kallithrakas-Kontos, S. Boghosian, M. Konsolakis, Ceria nanoparticles shape effects on the structural defects and surface chemistry: implications in CO oxidation by Cu/CeO_2 catalysts, Appl. Catal. B Environ. 230 (2018) 18–28.
[13] L. Pastor-Pérez, V. Belda-Alcázar, C. Marini, M.M. Pastor-Blas, A. Sepúlveda-Escribano, E.V. Ramos-Fernandez, Effect of cold Ar plasma treatment on the catalytic performance of Pt/CeO_2 in water-gas shift reaction (WGS), Appl. Catal. B Environ. 225 (2018) 121–127.
[14] J. Qi, K. Zhao, G. Li, Y. Gao, H. Zhao, R. Yu, Z. Tang, Multi-shelled CeO_2 hollow microspheres as superior photocatalysts for water oxidation, Nanoscale 6 (2014) 4072–4077.
[15] C. Li, X. Tang, H. Yi, L. Wang, X. Cui, C. Chu, J. Li, R. Zhang, Q. Yu, Rational design of template-free MnO_x-CeO_2 hollow nanotube as de-NO_x catalyst at low temperature, Appl. Surf. Sci. 428 (2018) 924–932.
[16] J. Zhang, Y. Cao, C.A. Wang, R. Ran, Design and preparation of MnO_2/CeO_2–MnO_2 double-shelled binary oxide hollow spheres and their application in CO oxidation, ACS Appl. Mater. Interfaces 8 (2016) 8670–8677.
[17] M. Sasidharan, N. Gunawardhana, M. Yoshio, K. Nakashima, CeO_2 hollow nanospheres as anode material for lithium ion batteries, Chem. Lett. 41 (2012) 386–388.
[18] K. Yoon, Y. Yang, P. Lu, D. Wan, H.C. Peng, K.S. Masias, P.T. Fanson, C.T. Campbell, Y. Xia, A highly reactive and sinter-resistant catalytic system based on platinum nanoparticles embedded in the inner surfaces of CeO_2 hollow fibers, Angew. Chem. Int. Ed. 51 (2012) 9543–9546.
[19] J. Zhang, M. Gong, C. Tian, C.A. Wang, Facile synthesis of well-defined CeO_2 hollow spheres with a tunable pore structure, Ceram. Int. 42 (2016) 6088–6093.
[20] C. Liu, H. Sun, J. Qian, Z. Chen, Y. Lv, F. Chen, X. Lu, Z. Wu, Biotemplating synthesis and photocatalytic activities of N-doped CeO_2 microcapsule tailored by hemerocallis pollen, Adv. Powder Technol. 28 (2017) 2741–2746.
[21] D. Zhang, Y. Qian, L. Shi, H. Mai, R. Gao, J. Zhang, W. Yu, W. Cao, Cu-doped CeO_2 spheres: synthesis, characterization, and catalytic activity, Catal. Commun. 26 (2012) 164–168.
[22] A.D. Liyanage, S.D. Perera, K. Tan, Y. Chabal, K.J. Balkus, Synthesis, characterization, and photocatalytic activity of Y-doped CeO_2 nanorods, ACS Catal. 4 (2014) 577–584.
[23] J. Xu, B. Xue, Y.M. Liu, Y.X. Li, Y. Cao, K.N. Fan, Mesostructured Ni-doped ceria as an efficient catalyst for styrene synthesis by oxidative dehydrogenation of ethylbenzene, Appl. Catal. Gen. 405 (2011) 142–148.
[24] Q. Shen, L. Zhang, N. Sun, H. Wang, L. Zhong, C. He, W. Wei, Y. Sun, Hollow MnO_x-CeO_2 mixed oxides as highly efficient catalysts in NO oxidation, Chem. Eng. J. 322 (2017) 46–55.
[25] Z. Wang, J. Qi, K. Zhao, L. Zong, Z. Tang, L. Wang, R. Yu, Controlled synthesis of highly active Au/CeO_2 nanotubes for CO oxidation, Mater. Chem. Front. 1 (2017) 1629–1634.
[26] Z. Li, H. Wang, W. Zhao, X. Xu, Q. Jin, J. Qi, R. Yu, D. Wang, Enhanced catalytic activity of Au-CeO_2/Al_2O_3 monolith for low-temperature CO oxidation, Catal. Commun. 129 (2019) 105729–105733.
[27] H. Wang, D. Mao, J. Qi, Q. Zhang, X. Ma, S. Song, L. Gu, R. Yu, D. Wang, Hollow multishelled structure of heterogeneous Co_3O_4-CeO_{2-x} nanocomposite for CO catalytic oxidation, Adv. Funct. Mater. 29 (2019) 1806588–1806596.
[28] W. Cai, Y. Zhao, M. Chen, X. Jiang, H. Wang, M. Ou, S. Wan, Q. Zhong, The formation of 3D spherical Cr-Ce mixed oxides with roughness surface and their enhanced low-temperature NO oxidation, Chem. Eng. J. 333 (2018) 414–422.
[29] S. Ijaz, M.F. Ehsan, M.N. Ashiq, N. Karamat, T. He, Preparation of CdS@CeO_2 core/shell composite for photocatalytic reduction of CO_2 under visible-light irradiation, Appl. Surf. Sci. 390 (2016) 550–559.
[30] B. Delley, An all-electron numerical method for solving the local density functional for polyatomic molecules, J. Chem. Phys. 92 (1990) 508–517.
[31] B. Delley, From molecules to solids with the DMol3 approach, J. Chem. Phys. 113 (2000) 7756–7763.
[32] J.P. Perdew, K. Burke, M. Ernzerhof, Generalized gradient approximation made simple, Phys. Rev. Lett. 77 (1996) 3865–3868.
[33] R. Murugan, G. Ravi, G. Vijayaprasath, S. Rajendran, M. Thaiyan, M. Nallappan, M. Gopalan, Y. Hayakawa, Ni-CeO_2 spherical nanostructures for magnetic and electrochemical supercapacitor applications, Phys. Chem. Chem. Phys. 19 (2017) 4396–4404.
[34] S. Brunauer, L.S. Deming, W.E. Deming, E. Teller, On a theory of the van der Waals adsorption of gases, J. Am. Chem. Soc. 62 (1940) 1723–1732.
[35] K.S.W. Sing, D.H. Everett, R.A.W. Haul, L. Moscou, R.A. Pierotti, J. Rouquérol, T. Siemieniewska, Reporting physisorption data for gas/solid systems with special reference to the determination of surface area and porosity, Pure Appl. Chem. 57 (1985) 603–619.
[36] W. Cai, Q. Zhong, W. Zhao, Y. Bu, Focus on the modified $Ce_xZr_{1-x}O_2$ with the rigid benzene-muti-carboxylate ligands and its catalysis in oxidation of NO, Appl. Catal. B Environ. 158–159 (2014) 258–268.
[37] W. Cai, Q. Zhong, W. Zhao, Solvent effects on formation of Cr-doped $Ce_{0.2}Zr_{0.8}O_2$ synthesized with cinnamic acid and their catalysis in oxidation of NO, Chem. Eng. J. 246 (2014) 328–336.
[38] W. Cai, Q. Zhong, J. Ding, Y. Bu, Solvent effects during the synthesis of Cr/$Ce_{0.2}Zr_{0.8}O_2$ catalysts and their activities in NO oxidation, Chem. Eng. J. 270 (2015) 1–8.
[39] Y. Wang, B. Li, C. Zhang, L. Cui, S. Kang, X. Li, L. Zhou, Ordered mesoporous CeO_2-TiO_2 composites: highly efficient photocatalysts for the reduction of CO_2 with H_2O under simulated solar irradiation, Appl. Catal. B Environ. 130 (2013) 277–284.
[40] X. Shi, S. Ji, K. Wang, Oxidative dehydrogenation of ethane to ethylene with carbon dioxide over Cr-Ce/SBA-15 catalysts, Catal. Lett. 125 (2008) 331–339.
[41] K. Takehira, Y. Ohishi, T. Shishido, T. Kawabata, K. Takaki, Q. Zhang, Y. Wang, Behavior of active sites on Cr-MCM-41 catalysts during the dehydrogenation of propane with CO_2, J. Catal. 224 (2004) 404–416.
[42] L.J. Liu, B. Liu, L.H. Dong, J. Zhu, H.Q. Wan, K.Q. Sun, B. Zhao, H.Y. Zhu, L. Dong, Y. Chen, In situ FT-infrared investigation of CO or/and NO interaction with CuO/$Ce_{0.67}Zr_{0.33}O_2$ catalysts, Appl. Catal. B Environ. 90 (2009) 578–586.
[43] Z. Zhao, X.G. Yang, Y. Wu, Comparative study of nickel-based perovskite-like mixed oxide catalysts for direct decomposition of NO, Appl. Catal. B Environ. 8 (1996) 281–297.
[44] I. Atribak, N. Guillén-Hurtado, A. Bueno-López, A. García-García, Influence of the physic-chemical properties of CeO_2-ZrO_2 mixed oxides on the catalytic oxidation of NO to NO_2, Appl. Surf. Sci. 256 (2010) 7706–7712.
[45] W. Cai, Q. Zhong, S. Zhang, J. Zhang, Effects of Cr on the NO oxidation over the ceria-zirconia solid solution, RSC Adv. 3 (2013) 7009–7015.
[46] B.Q. Jiang, Z.B. Wu, Y. Liu, S.C. Lee, W.K. Ho, DRIFT study of the SO_2 effect on low temperature SCR reaction over Fe-Mn/TiO_2, J. Phys. Chem. C 114 (2010) 4961–4965.
[47] H.Y. Huang, R.T. Yang, Removal of NO by reversible adsorption on Fe-Mn based transition metal oxides, Langmuir 17 (2001) 4997–5003.
[48] J.A. Rodriguez, T. Jirsak, J. Dvorak, S. Sambasivan, D. Fischer, Reaction of NO_2 with Zn and ZnO: photoemission, XANES, and density functional studies on the formation of NO_3, J. Phys. Chem. B 104 (2000) 319–328.
[49] X. Wang, H.Y. Chen, W.M.H. Sachtler, Mechanism of the selective reduction of NO_x over Co/MFI: comparison with Fe/MFI, J. Catal. 197 (2001) 281–291.
[50] A. Bensalem, J.C. Muller, F.B. Verduraz, From bulk CeO_2 to supported cerium-oxygen clusters: a diffuse reflectance approach, J. Chem. Soc. Faraday. Trans. 88 (1992) 153–154.
[51] B.M. Reddy, P. Bharali, G. Thrimurthulu, P. Saikia, L. Katta, S.E. Park, Catalytic efficiency of ceria-zirconia and ceria-hafnia nanocomposite oxides for soot

oxidation, Catal. Lett. 123 (2008) 327–333.
[52] A. Bensalem, F.B. Verduraz, M. Delamar, G. Bugli, Preparation and characterization of highly dispersed silica-supported ceria, Appl. Catal. 121 (1995) 81–93.
[53] C.P. Poole, J.F. Itzel, Optical reflection spectra of chromia-alumina, J. Chem. Phys. 39 (1963) 3445–3455.
[54] T. Tachikawa, T. Ochi, Y. Kobori, Crystal-face-dependent charge dynamics on a $BiVO_4$ photocatalyst revealed by single-particle spectroelectrochemistry, ACS Catal. 6 (2016) 2250–2256.
[55] S. Wan, M. Ou, Q. Zhong, S. Zhang, W. Cai, Supramolecular synthesis of multifunctional holey carbon nitride nanosheet with high-efficiency photocatalytic performance, Adv. Opt. Mater. 5 (2017) 1700536–1700546.
[56] N.J. Bell, Y.H. Ng, A. Du, H. Coster, S.C. Smith, R. Amal, Understanding the enhancement in photoelectrochemical properties of photocatalytically prepared TiO_2-reduced graphene oxide composite, J. Phys. Chem. C 115 (2011) 6004–6009.